



Publication Year	2022
Acceptance in OA @INAF	2022-03-28T09:39:53Z
Title	Macro and micro structures of pebble-made cometary nuclei reconciled by seasonal evolution
Authors	CIARNIELLO, Mauro; FULLE, Marco; RAPONI, Andrea; FILACCHIONE, GIANRICO; CAPACCIONI, FABRIZIO; et al.
DOI	10.1038/s41550-022-01625-y
Handle	http://hdl.handle.net/20.500.12386/31932
Journal	NATURE ASTRONOMY

Supplementary information

Macro and micro structures of pebble-made cometary nuclei reconciled by seasonal evolution

In the format provided by the authors and unedited

1 **Supplementary Information of**

2 **Macro and micro structures of pebble-made cometary**

3 **nuclei reconciled by by seasonal evolution**

4 **Mauro Ciarniello^{1,*}, Marco Fulle², Andrea Raponi¹, Gianrico Filacchione¹, Fabrizio**
5 **Capaccioni¹, Alessandra Rotundi^{3,1}, Giovanna Rinaldi¹, Michelangelo Formisano¹,**
6 **Gianfranco Magni¹, Federico Tosi¹, Maria Cristina De Sanctis¹, Maria Teresa Capria¹,**
7 **Andrea Longobardo¹, Pierre Beck⁴, Sonia Fornasier^{5,6}, David Kappel^{7,8}, Vito Mennella⁹,**
8 **Stefano Mottola⁷, Batiste Rousseau¹, and Gabriele Arnold⁷**

9 ¹Istituto Nazionale di AstroFisica – Istituto di Astrofisica e Planetologia Spaziali (INAF-IAPS), Rome, Italy.

10 ²INAF - Osservatorio Astronomico, Trieste, Italy.

11 ³Università degli Studi di Napoli Parthenope, Dip. di Scienze e Tecnologie, Naples, Italy.

12 ⁴Université Grenoble Alpes, CNRS, IPAG, Grenoble, France.

13 ⁵Institut Universitaire de France (IUF), Paris, France.

14 ⁶LESIA, Observatoire de Paris, Université PSL, CNRS, Université de Paris, Sorbonne Université, Meudon,
15 France.

16 ⁷Institute of Planetary Research, German Aerospace Center (DLR), Berlin, Germany.

17 ⁸Institute of Physics and Astronomy, University of Potsdam, Potsdam, Germany

18 ⁹INAF—Osservatorio Astronomico di Capodimonte, Naples, Italy.

19 *mauro.ciarniello@inaf.it

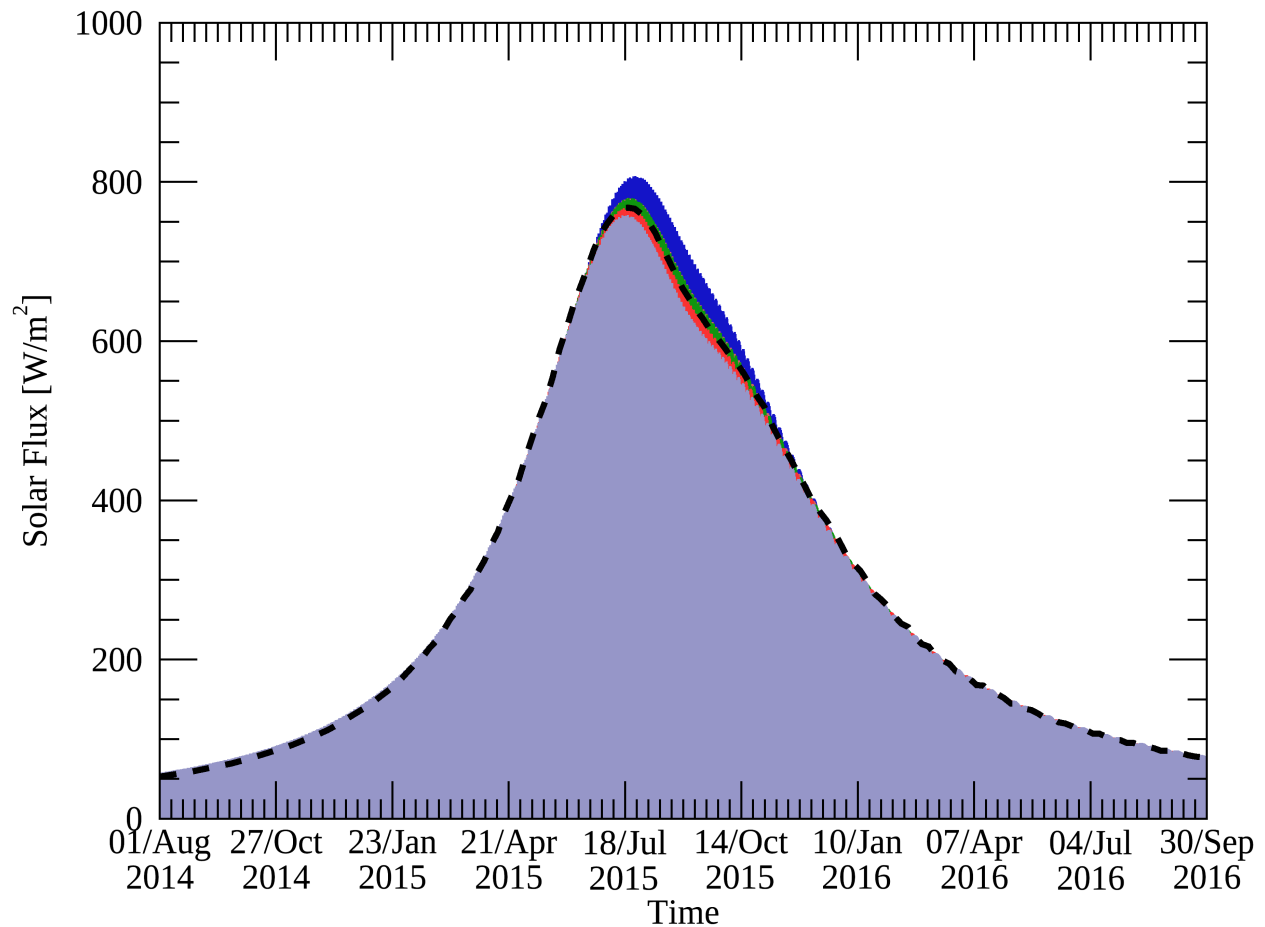
20 **Supplementary tables and figures cited in the main article**

Period	MTP	Avg. heliocentric distance	Spatial resolution
1 August 2014 - 2 September 2014	MTP006	3.54 au	13-98 m/pixel
8 April 2015 - 5 May 2015	MTP015	1.83 au	23-39 m/pixel
25 August 2015 - 22 September 2015	MTP020	1.28 au	78-107 m/pixel
17 November 2015 - 15 December 2015	MTP023	1.78 au	25-36 m/pixel
31 May 2016 - 28 June 2016	MTP030	3.20 au	3-8 m/pixel

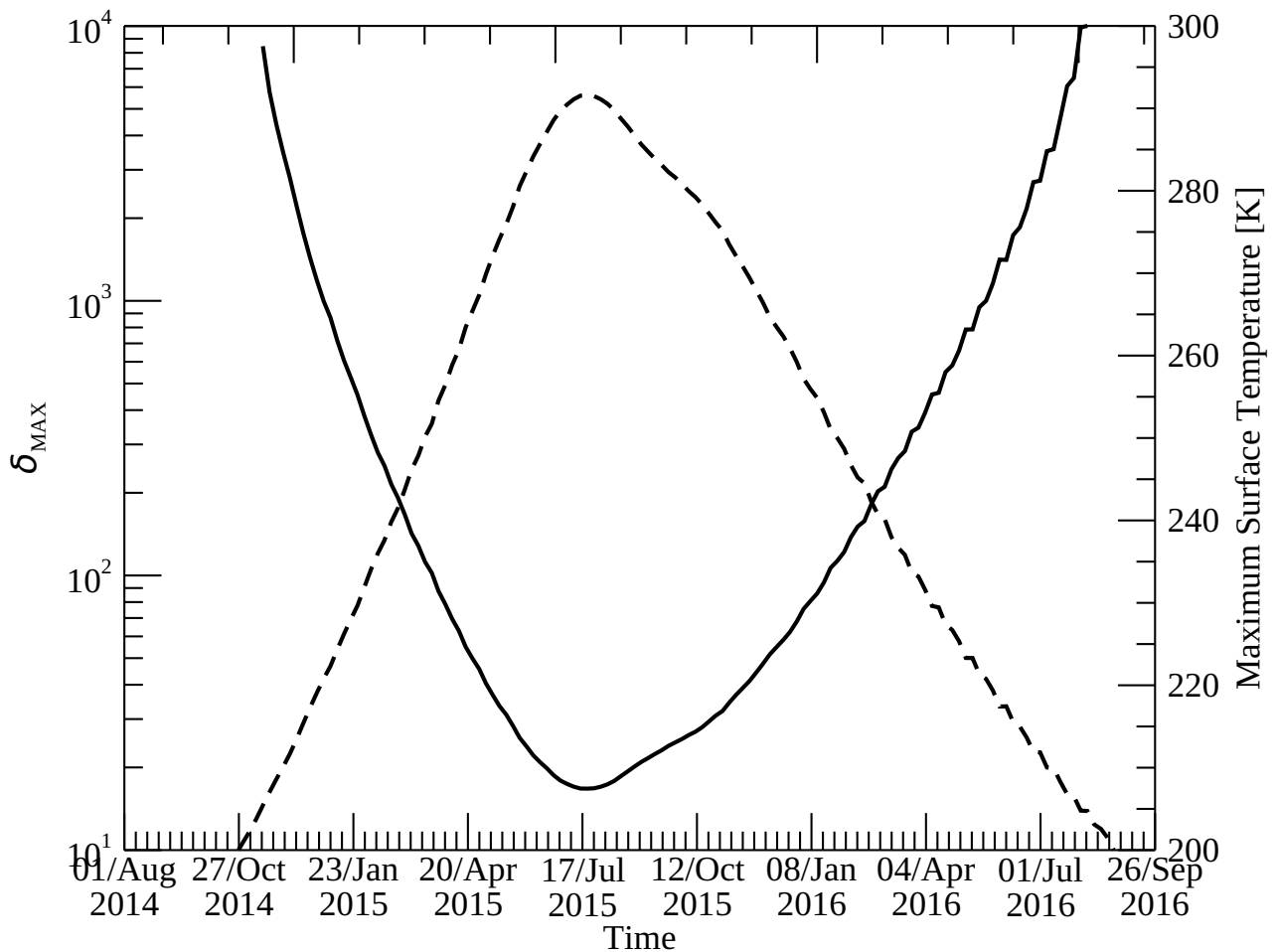
Supplementary Table 1. Timing of the spectral-slope maps of Fig. 1. The corresponding Rosetta Medium Term Planning (MTP) phases are indicated, along with the comet average heliocentric distance and the spatial resolution of VIRTIS observations.

ROI	Latitude	Longitude	Morphological region
1	$-30^{\circ} - 0^{\circ}$	$120^{\circ} - 150^{\circ}$	Imhotep
2	$15^{\circ} - 30^{\circ}$	$135^{\circ} - 150^{\circ}$	Imhotep/Ash
3	$-15^{\circ} - 0^{\circ}$	$255^{\circ} - 270^{\circ}$	Hapi/Seth
4	$0^{\circ} - 10^{\circ}$	$350^{\circ} - 359^{\circ}$	Hatmehit
5	$-75^{\circ} - -60^{\circ}$	$120^{\circ} - 150^{\circ}$	Imhotep/Bes

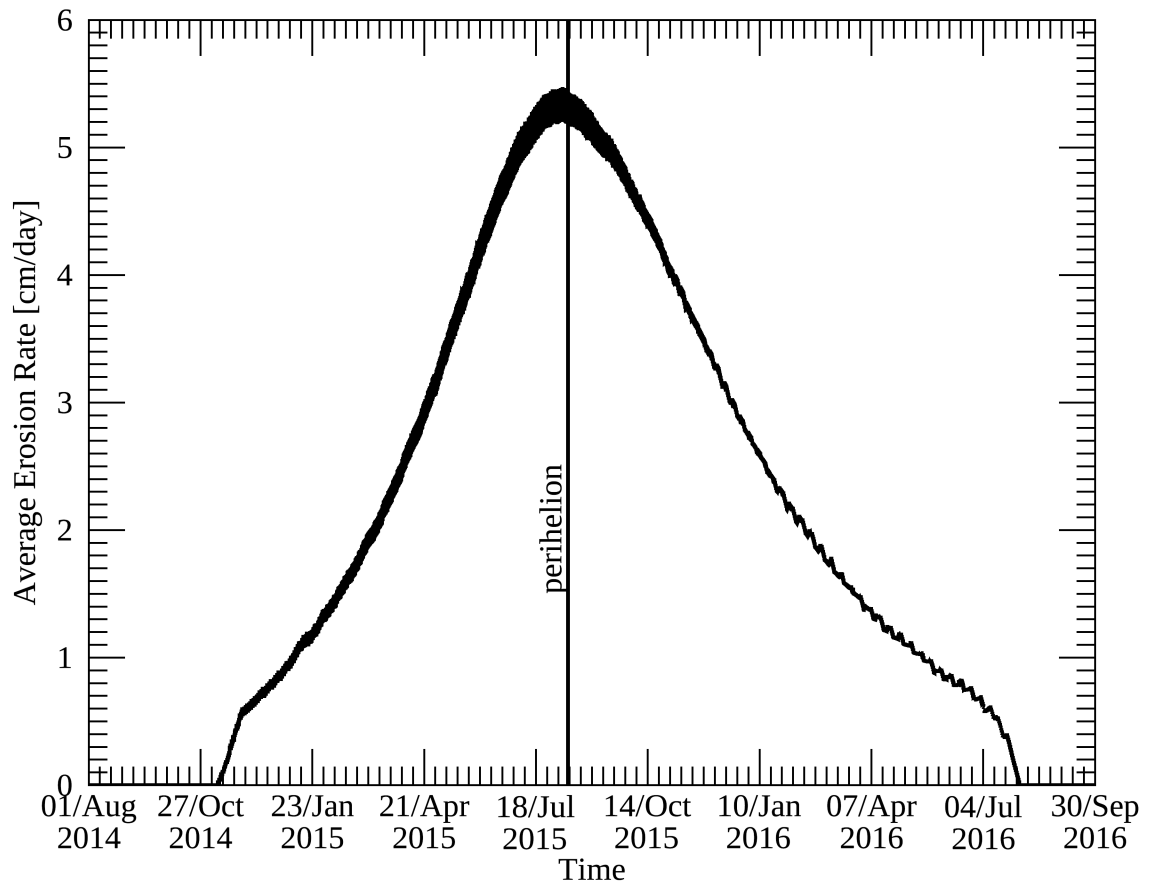
Supplementary Table 2. Latitude and longitude intervals of the ROIs defined in Fig. 1. The last column indicates the morphological regions where the ROIs are located, following the regional nomenclature from¹.



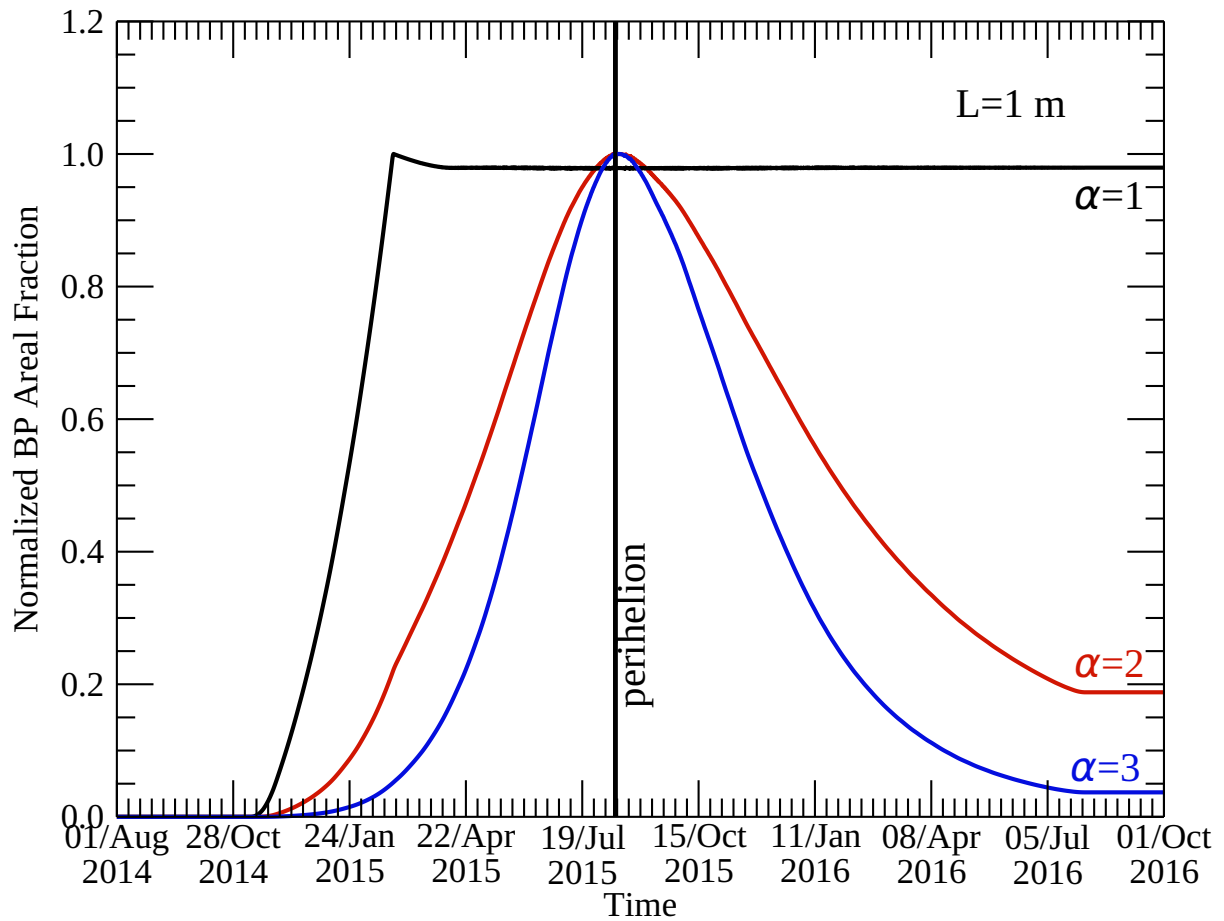
Supplementary Figure 1. Insolation over the ROI 1. The incident solar flux at the surface from August 2014 to September 2016 has been computed at five positions, corresponding to the ROI corners and centre by means of the SPICE tool². This result in five different curves that are superimposed in the plot (as a consequence only four of them are visible). The insolation curves account also for the diurnal cycle on the comet surface, thus, in a single rotation the Solar flux on the ROI 1 is zero at night and maximum at noon. Note that in the present visualisation such day-night variability is not resolved. The curves of the five positions have been averaged to produce an average insolation curve of the ROI 1 (not shown). We report, as a black dashed line, the upper envelope of this curve, computed over a running box of approximately 10 comet rotations, representing the temporal evolution of the maximum flux over the ROI 1.



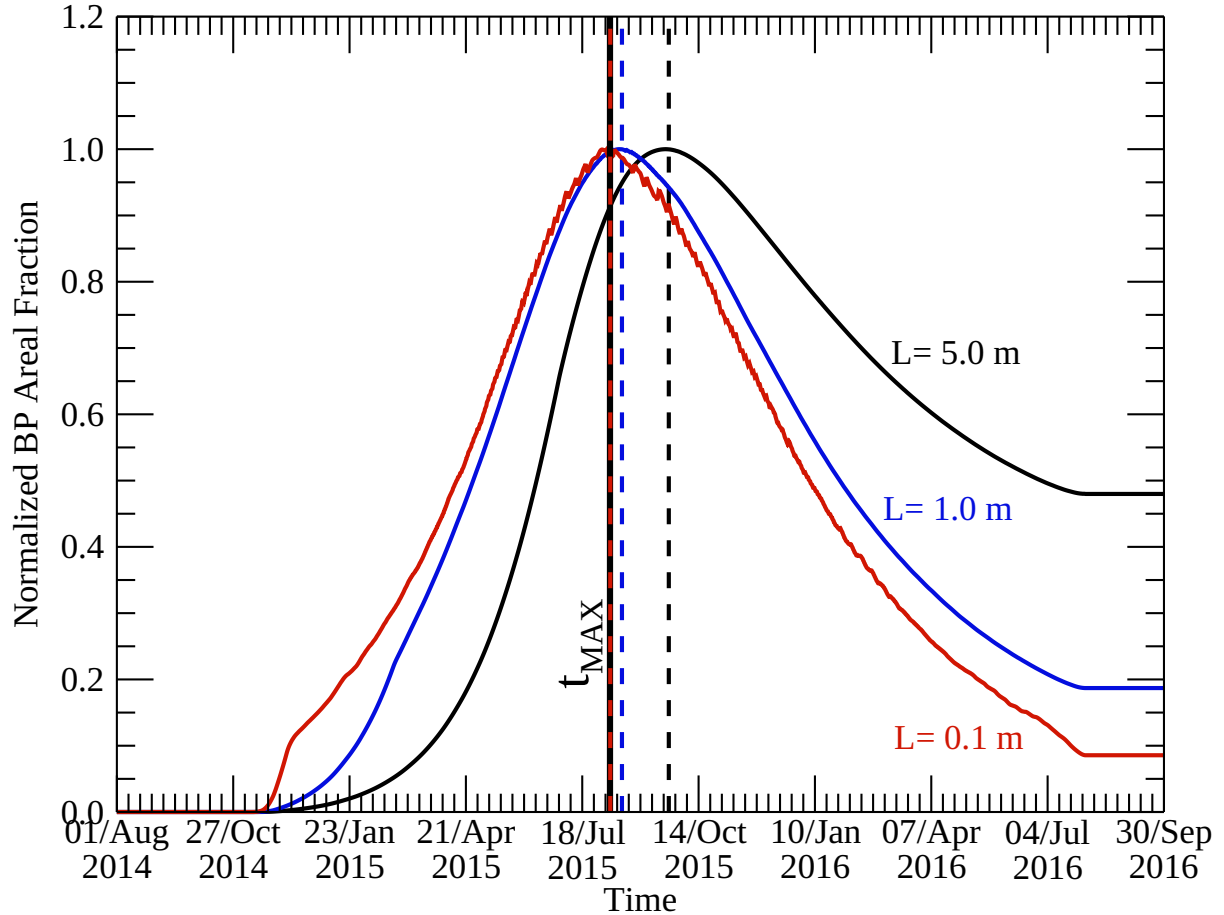
Supplementary Figure 2. δ_{MAX} and maximum surface temperature from August 2014 to September 2016 for the ROI 1. δ_{MAX} (solid line) is not defined before November 2014 and approximately after August 2016, as surface temperature in the ROI 1 is < 205 K and cannot sustain water-driven activity³. The maximum surface temperature (dashed line) is computed from August 2014 to September 2016 by assuming the maximum solar flux over the ROI 1 shown in Supplementary Fig. 1.



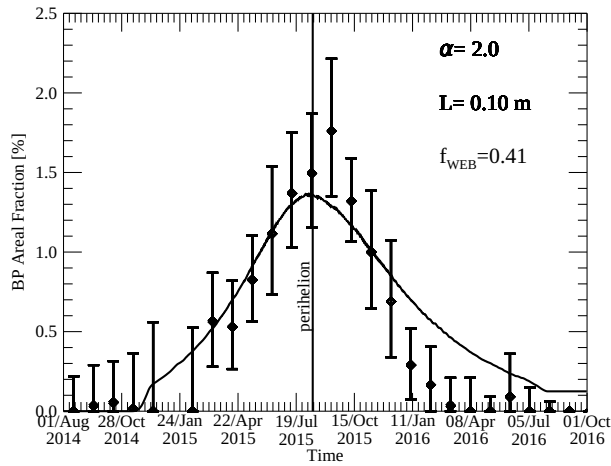
Supplementary Figure 3. Average erosion rate in the ROI 1. The curve is obtained after averaging over a 10-day running box.



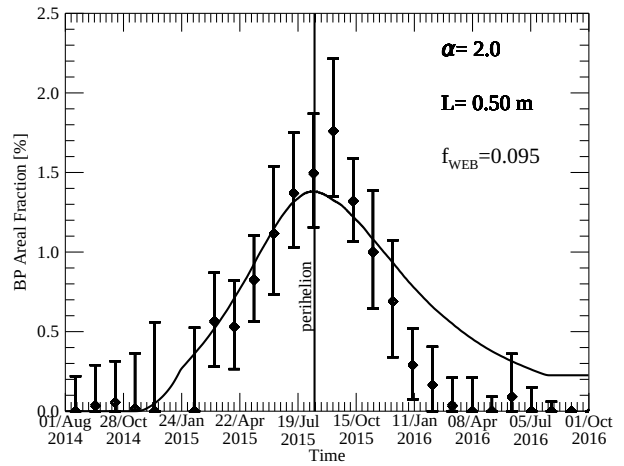
Supplementary Figure 4. Temporal evolution of the BP areal fraction for different values of α . The normalized BP areal fraction is reported versus time, for different behaviors of f_{CO_2} as a function of the index α . For each simulation we adopted $f_{WEB} = 0.5$ and $K = 0.0001 \text{ h}^{-1}$ and WEB size $L = 1 \text{ m}$ and $L_c = 0.1 \text{ m}^4$. Such values allow the simulations to be far from a saturation regime, with maximum values of $BP(t) \ll f_{WEB}$.



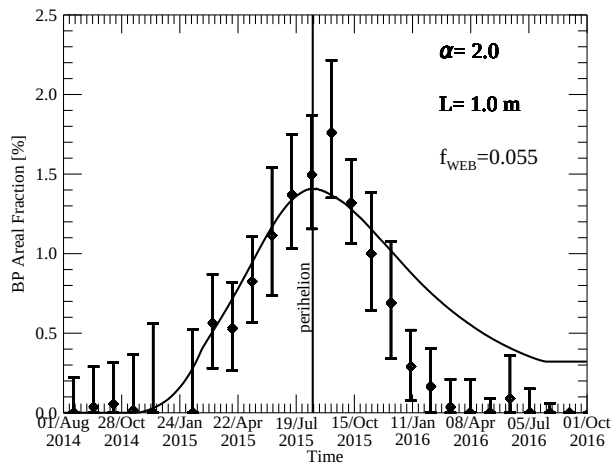
Supplementary Figure 5. Normalized $BP(t)$ curves for different values of L . In these simulations we adopted $L_c \ll L$, $K = 0.0001 \text{ h}^{-1}$ and $f_{WEB} = 0.5$. For illustrative purposes, the selected values of L_c and K are chosen to provide a negligible effect of the additional erosion of the BPs from CO_2 activity. The positions of the local maxima for the different cases are indicated by dashed lines. The position of t_{MAX} is indicated with a solid line. The derived delay of the $BP(t)$ maximum with respect to the maximum in the activity is ≈ 1.5 days, ≈ 10 days and ≈ 46 days for $L = 0.1$ m, $L = 1$ m and $L = 5$ m, respectively. The delays, as estimated with Eq. 13 and $E(t_{MAX}) = 5.5 \text{ cm/day}$ are ≈ 0.9 days, ≈ 9 days and ≈ 46 days, in good agreement with the results from the numerical integration for $L = 0.1$ m, $L = 1$ m and $L = 5$ m, respectively. All the curves reach a plateau at the end of the investigated time interval. These correspond to the cessation of water-driven erosion ($E(t) = 0$), which preserves the residual BPs in the simulation. However, in this regime, water ice sublimation, although not able to erode the surface, would cause dehydration of BPs³, which eventually disappear. This effect is not included in the present model.



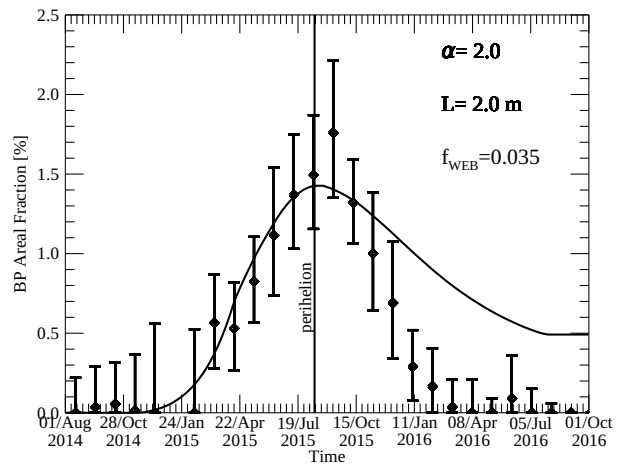
(a)



(b)

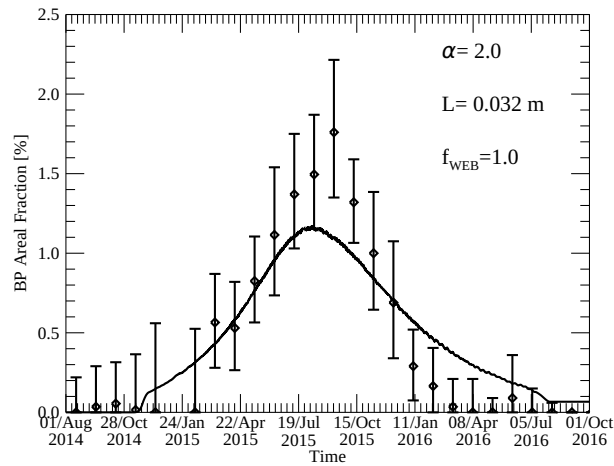


(c)

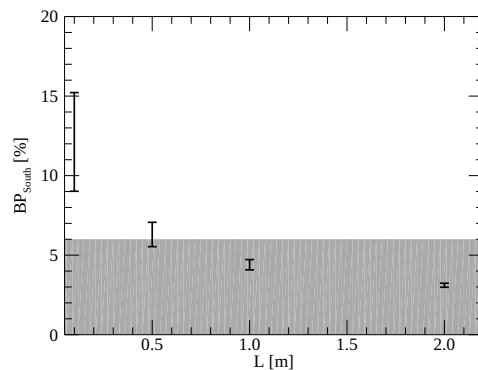


(d)

Supplementary Figure 6. Best fit models of the BP temporal evolution over the ROI 1. The BP areal fraction (diamonds and error bars), as derived from VIRTIS data including the corresponding uncertainties, is compared with models (solid lines) for $L=0.1, 0.5, 1, 2 \text{ m}$ and $\alpha=2$. The best fit values of f_{WEB} are reported.



Supplementary Figure 7. Characterisation of the WEB size lower limit. The temporal evolution of the BP areal fraction over the ROI 1 (diamonds and error bars), as derived from VIRTIS data including the corresponding uncertainties, is compared with an ideal model assuming $f_{WEB} = 1$ and $\alpha = 2$. The value of L is chosen as the smallest one for which the obtained evolution of $BP(t)$ is still considered compatible with observations.



Supplementary Figure 8. BP_{South} as a function of the WEB size L . For each point the bars span from a minimum to a maximum value, corresponding to the extreme BP_{South} values obtained by combining $E_{tot} = 4$ m, 10 m, and $L_c = 0.1$ m, 0.13 m. The grey band represents BP_{South} values compatible with the 6% upper limit of water-active areas in the active southern hemisphere.

21 1 Spectral-slope computation and mapping

22 Maps of spectral slope are produced following the approach described in ref.⁵ from photometrically
23 reduced data⁶, by converting the calibrated radiance factor ($I/F=\pi \times reflectance$) measured by VIRTIS-M
24 nucleus observations into spectral single scattering albedo (SSA or w , Eq. 10)⁷. Such approach allows
25 us to minimise the spectrophotometric effects induced by the variation of observation geometry on the
26 surface reflectance and permits to compare acquisitions taken under different observation geometries
27 and at different times. Following the method adopted in previous studies^{5,8}, for each SSA spectrum the
28 spectral slope at visible wavelengths is computed as

$$S_{VIS} = \left(\frac{\Delta SSA}{\Delta \lambda} \right)_{0.55-0.8} \frac{100\%}{SSA_{0.55}}, \quad (1)$$

29 where $\left(\frac{\Delta SSA}{\Delta \lambda} \right)_{0.55-0.8}$ is the slope of a linear fit in the 0.55-0.8 μm interval, and $SSA_{0.55}$ is the single
30 scattering albedo at 0.55 μm . Note that for the S_{VIS} computation we express wavelength in 100-nm unit,
31 thus the S_{VIS} unit is $\%/(100 \text{ nm})$.

32 2 Correction of the effect of calibration residuals on S_{VIS}

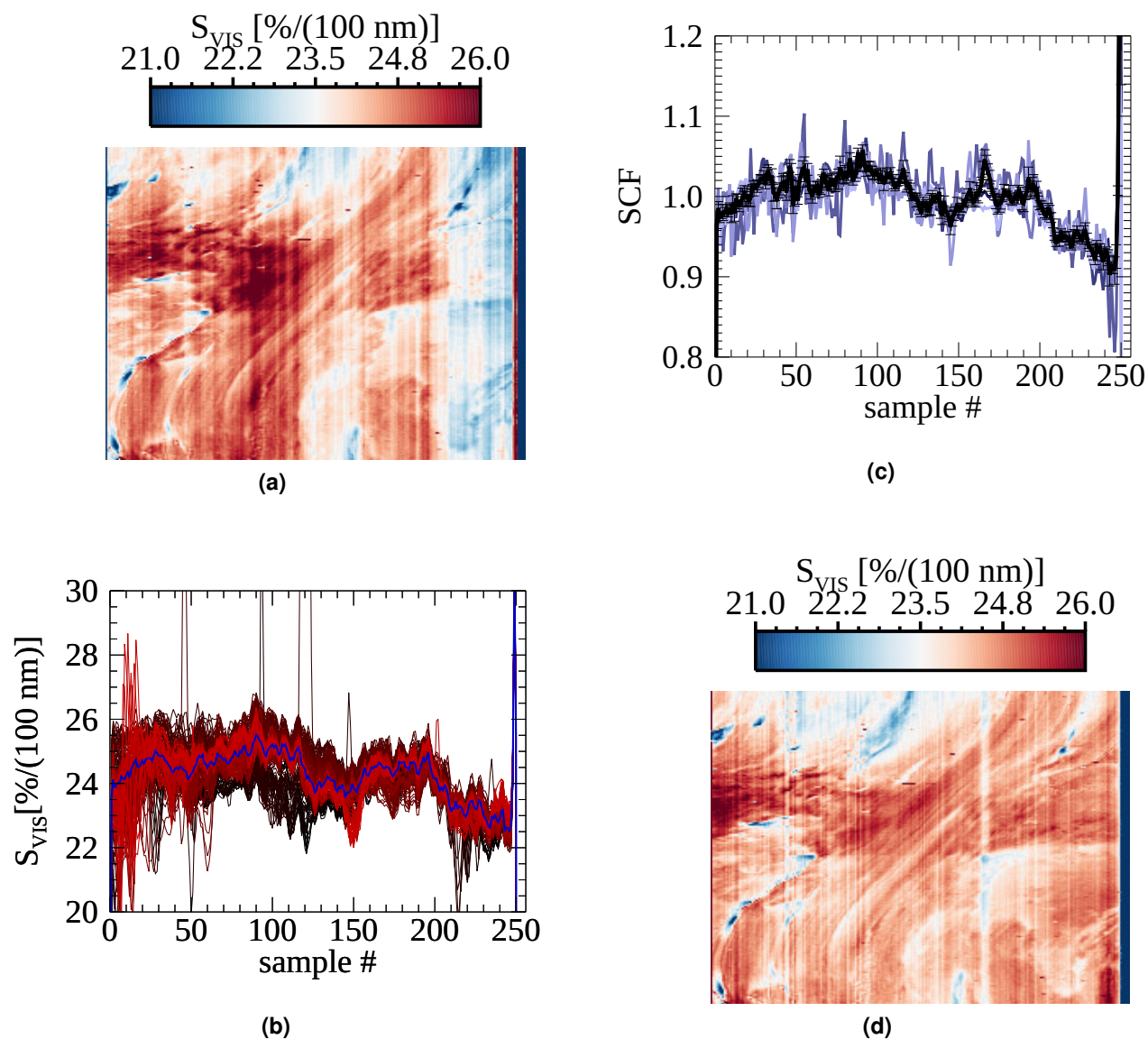
33 VIRTIS-M observations are performed by acquiring sequences of *lines*, which correspond to images of
34 the target through the spectrometer slit. The different *lines*, composed of 256 pixels (*samples*) each, are
35 put together to produce the final VIRTIS-M bidimensional image at a given wavelength⁹. An analysis
36 of the SSA spectral slope (S_{VIS}) from VIRTIS-M hyperspectral images (*cubes*), revealed two residual
37 calibration issues which manifested as 1) a systematic correlation of S_{VIS} with the sample position in the
38 VIS detector and 2) a positive correlation of S_{VIS} with the VIS detector (CCD) temperature. Below, we
39 describe the empirical approach we adopted to correct the derived spectral slope in the visible for such
40 effects.

41 2.1 Correction for S_{VIS} sample dependence

42 In order to model and then correct the observed dependence of S_{VIS} on the sample position (s) we selected
43 six VIRTIS-M hyperspectral images (see Supplementary Table 3) where the instrument FOV (field of
44 view) was fully occupied by the nucleus and with limited occurrence of shadows. Each hyperspectral
45 cube has been reduced to SSA (Eq. 10) and converted to a S_{VIS} image by computing the spectral slope
46 for each pixel (Supplementary Fig. 9a). For each image i , a median $S_{VIS}^i(s)$ profile along the sample
47 direction has been derived, by computing the median spectral-slope value for pixels corresponding to
48 different lines at the same sample (Supplementary Fig. 9b). Each of the different $S_{VIS}^i(s)$ median profiles
49 has been normalised to its median value along the samples obtaining a Slope Correction Factor ($SCF^i(s)$)
50 profile. Finally, the median of the $SCF^i(s)$ profiles from the different images has been computed at each
51 sample position to obtain a final slope correction factor $SCF(s)$ (Supplementary Fig. 9c). With the aim
52 to correct the derived spectral-slope images for the systematic dependence on the sample position, the
53 derived value of the spectral slope at a given s is divided by the value of the $SCF(s)$ at the same sample
54 (Supplementary Fig. 9d).

55 2.2 Correction for S_{VIS} instrument temperature dependence

56 A comparison among VIRTIS-M spectral-slope images acquired in sequence evidenced that the average
57 value of the spectral slope in each image is positively correlated with the VIS detector (CCD) temperature
58 (also referred to as focal plane temperature) at the time of acquisition. Starting from the beginning of



Supplementary Figure 9. Characterisation and correction of the S_{VIS} sample dependence. a) S_{VIS} image as derived from VIRTIS-M hyperspectral cube V_00418865371. Surface features deformation is due to the spacecraft movement relative to the nucleus surface during acquisition. Notice the bluish band on the right side of the image corresponding to samples with systematically lower spectral slope. b) $S_{VIS}(s)$ profiles from each line of the image (curves with different red colour tones) and the corresponding median profile (blue thick curve). c) $SCF^i(s)$ profiles for each observation of Supplementary Table 3 and median $SCF(s)$ (black thick curve) with formal errors. d) S_{VIS} image after the application of the Slope Correction Factor.

59 May 2015, corresponding to the end of the operations of the cryocooler used to cool down the IR detector,
 60 the VIS channel acquisition mode has been reconfigured to operate with longer integration and repetition
 61 times. This strategy has allowed the SNR of the VIS channel to be improved at expenses of a progressive
 62 warming of the CCD and higher operating temperatures, resulting in a systematic change of the detector
 63 response. In the following we report about the strategy used to correct this effect and homogenise the

Cube	Date	Number of lines	Target distance [km]
V1_00418865371	9 Apr 2016	202	28.2
V1_00430446438	22 Aug 2016	120	4.9
V1_00431457438	2 Sept 2016	63	4.2
V1_00431742197	6 Sept 2016	57	3.5
V1_00433297397	24 Sept 2016	58	3.9
V1_00433665027	28 Sept 2016	82	21.1

Supplementary Table 3. List of the hyperspectral cubes selected to develop the S_{VIS} sample dependence correction, and corresponding observation circumstances.

64 response across the entire dataset, an operation necessary to compare data collected during the entire
65 duration of the mission. In Supplementary Fig. 10 a sequence of images, acquired in ≈ 4.5 hours, with a
66 single cube acquisition time of approximately 30 minutes, is shown. A clear increase of the measured
67 spectral slope across the whole illuminated nucleus can be observed, from the first to the last acquisition,
68 along with the focal plane temperature. In order to correct for this effect, a statistical approach has been
69 developed to model the spurious increase of the measured spectral slope with temperature. To this purpose,
70 we assume that, for a given acquisition, the effect of the corresponding CCD temperature (T) on the
71 average of the computed spectral slope across the nucleus after photometric reduction, can be modelled by
72 a multiplicative term $f(T)$ according to the following relation

$$S_{VIS}(n, T) = S_{VIS}^*(n) \times f(T), \quad (2)$$

73 where the index n indicates the n th hyperspectral cube and $S_{VIS}^*(n)$ refers to the intrinsic average spectral
74 slope of the surface. We assume that S_{VIS}^* is not correlated with the CCD temperature, then, by averaging
75 over different images ($\langle \rangle_n$) acquired with the same T , we obtain the following relation

$$\langle S_{VIS}(n, T) \rangle_n = \langle S_{VIS}^*(n) \rangle_n \times f(T). \quad (3)$$

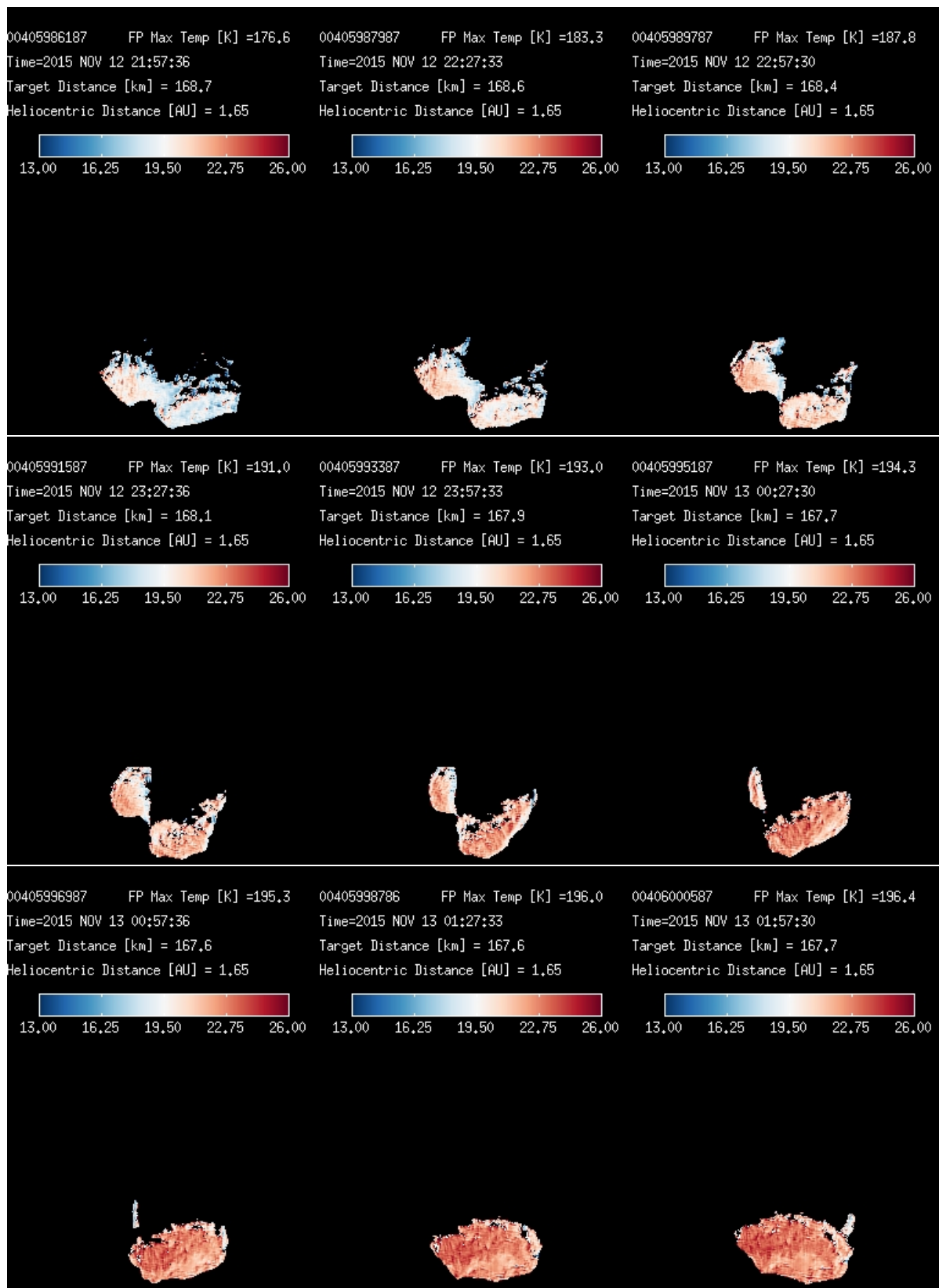
76 Given that the instrument was calibrated at a nominal operating focal plane temperature of 180 K we can
77 consider this temperature as the reference value at which the derived spectral slope is representative of the
78 intrinsic properties of the nucleus. Then we can set $f(180 \text{ K}) = 1$ which implies $S_{VIS}^*(n) = S_{VIS}(n, 180 \text{ K})$
79 and

$$\langle S_{VIS}(n, T) \rangle_n = \langle S_{VIS}(n, 180 \text{ K}) \rangle_n \times f(T), \quad (4)$$

80 where $\langle S_{VIS}(n, T) \rangle_n$ represents the average derived nucleus spectral slope as a function of the temperature
81 (slope-temperature profile), that, for brevity of notation, we rename as $S_{VIS}(T)$. It follows that Eq. 4 can
82 be now expressed as

$$S_{VIS}(T) = S_{VIS}(180 \text{ K}) \times f(T) \quad (5)$$

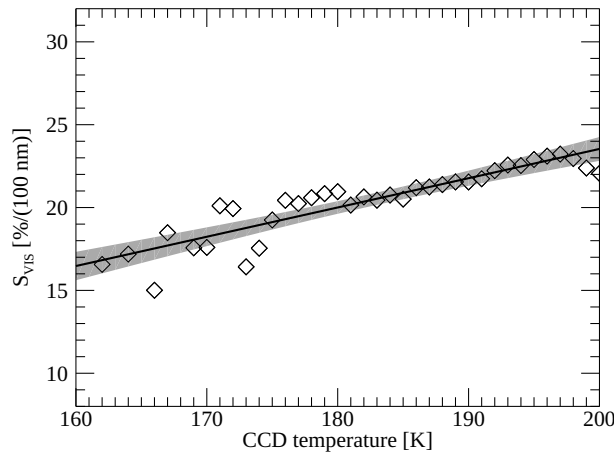
83 which provides a general relation between the computed VIS spectral slope, its reference value at $T = 180$
84 K, and the CCD temperature T during the acquisition. To estimate $f(T)$ and $S_{VIS}(180 \text{ K})$ in Eq. 5, a set
85 of 10^6 slope-temperature profiles has been generated from VIRTIS-M observations acquired with different
86 CCD temperatures in the $160 \text{ K} < T < 200 \text{ K}$ range. The slope-temperature profiles have been built with a
87 temperature sampling of $\Delta T = 1 \text{ K}$ by extracting randomly from the VIRTIS-M $S_{VIS}(n, T)$ distribution a
88 value of the VIS spectral slope for each temperature bin. Observations are taken from Rosetta Medium



Supplementary Figure 10. Effect of S_{VIS} dependence on the CCD temperature. Sequence of S_{VIS} images from cubes acquired between 12 and 13 November 2015. The acquisition of a single cube took approximately 30 minutes. Phase angle was $\approx 61^\circ$ for all the images, and additional observation circumstances are indicated. Between the first and the last acquisition, the instrument progressively warmed up, and the maximum focal plane temperature (FP Max Temp), where the CCD is located, increased from 176.6 K to 196.4 K. This produced a systematic increase of S_{VIS} across the nucleus. Colour bar values are given in $\%/(100 \text{ nm})$.

89 Term Planning (MTP) sequences MTP017, MTP018, MTP022, MTP023, MTP024, MTP025, MTP026,
 90 MTP028 which were performed under variable CCD temperature conditions and sampled different phases
 91 of the comet surface evolution. The 10^6 spectral-slope profiles have been modeled with a linear fit where
 92 $f(T) = A + BT$. We note that according to Eq. 5 the quantities derived from the linear fit are actually
 93 given by $S_{VIS}(180\text{ K}) \times A$ and $S_{VIS}(180\text{ K}) \times B$, which will be referred to as SA and SB , respectively. By
 94 fitting the different 10^6 slope-temperature profiles a distribution for SA and SB is obtained, from which
 95 we derived the average values $SA = (-11.8 \pm 3.5) \%/ (100\text{ nm})$ and $SB = (0.177 \pm 0.021) \%/ (100\text{ nm}$
 96 $\text{K})$. The final values for A , B , and $S_{VIS}(180\text{ K})$ are straightforwardly derived by imposing $f(180\text{ K}) = 1$.
 97 This gives $B = (1 - A)/(180\text{ K})$, from which it follows: $A = -0.5 \pm 0.17$, $B = (0.0088 \pm 0.00095)\text{ K}^{-1}$ and
 98 $S_{VIS}(180\text{ K}) = (20.001 \pm 0.028) \%/ (100\text{ nm})$. In Supplementary Fig. 11 we report the average of the 10^6
 99 spectral-slope temperature profiles, and Eq. 5 as computed with the estimated average values of SA and
 100 SB . It can be noted that the dependence of the computed spectral slope on the CCD temperature can be
 101 effectively described by a linear relation.

102 By using Eq. 5 and the results of the linear fit, the spectral slope for a given pixel $S_{VIS}^P(T)$ can be
 103 translated to its reference value at 180 K, $S_{VIS}^P(180\text{ K})$, by means of the simple relation $S_{VIS}^P(180$
 $\text{K}) = (S_{VIS}^P(T))/f(T)$. In Supplementary Fig. 12 we show the sequence of spectral-slope images of

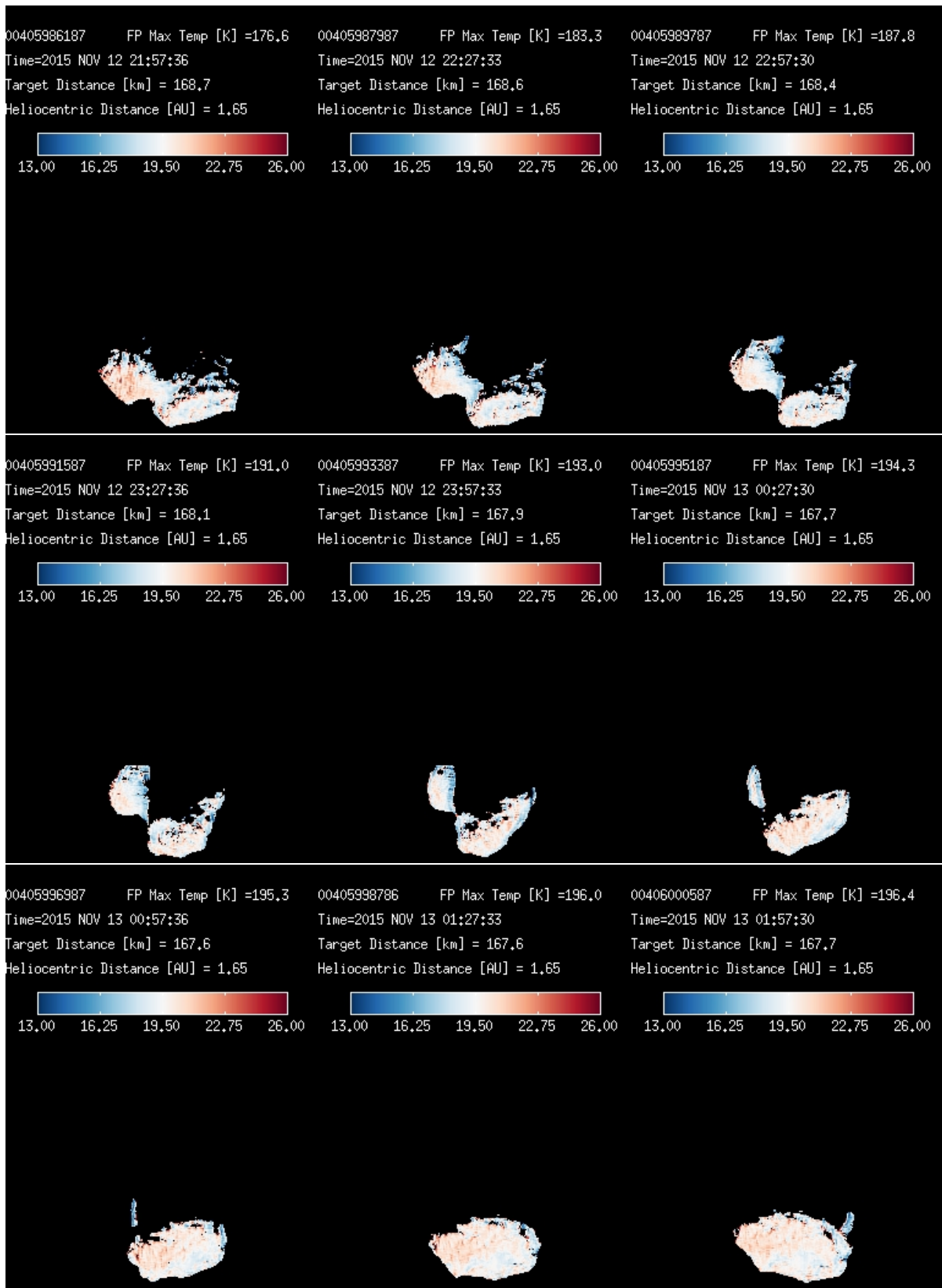


Supplementary Figure 11. S_{VIS} -CCD temperature average profile. S_{VIS} and the CCD temperature are correlated and their relation has been fitted with the linear model (black curve) of Eq. 5 and $SA = -11.8 \%/ (100\text{ nm})$ and $SB = 0.177 \%/ (100\text{ nm K})$. We indicate as a grey band the 98% confidence interval for the predicted values in the linear regression: at 200 K the width of the confidence interval is $\approx 6\%$ of the best fit value, and reduces to $\approx 4\%$ at 180 K. These can be considered as conservative estimates of the error on the correction for the spectral-slope dependency on the CCD temperature.

104
 105 Supplementary Fig. 10 after correcting for the CCD temperature dependence, demonstrating that the
 106 spurious increase of spectral slope with temperature has been properly corrected.

107 3 Spectral modelling

108 We describe the cometary surface as a geographical (or areal) mixture of the cometary dark terrain (being
 109 poor in water ice and having a low albedo) and BPs. The corresponding reflectance can then be expressed



Supplementary Figure 12. Correction of the S_{VIS} dependence on the CCD temperature. The same sequence of S_{VIS} images from Supplementary Fig. 10, after correction for the CCD temperature effect on the computed spectral slope. Colour bar values are given in $\%/(100 \text{ nm})$.

110 as a linear combination of the radiance factor of the dark terrain (I/F_{DT}) and of the BPs (I/F_{BP}):

$$I/F = (1 - f_{BP})I/F_{DT} + f_{BP}I/F_{BP}, \quad (6)$$

111 where f_{BP} is the areal fraction of BPs. By applying a simplified version of the Hapke model⁷ it has been
 112 shown⁶ that, far from the opposition effect region, the dark terrain radiance factor for comet 67P can be
 113 expressed as

$$I/F_{DT} = \frac{w_{DT}(\lambda)}{4} \frac{\mu_{0e}}{\mu_{0e} + \mu_e} \Pi_{DT}(\lambda, g) S(i, e, g, \bar{\theta}), \quad (7)$$

114 where the contribution of multiple scattering is considered negligible given the low albedo of the surface,
 115 and with i, e, g being the incidence, emission and phase angles, respectively, μ_{0e} and μ_e the effective cosines
 116 of the incidence and emission angle, $w_{DT}(\lambda)$ the single scattering albedo of the dark terrain, $\Pi_{DT}(\lambda, g)$
 117 the single particle phase function of the dark terrain and $S(i, e, g, \bar{\theta})$ the shadowing function of the surface,
 118 depending on the roughness parameter $\bar{\theta}$. Always referring to the Hapke theory, the radiance factor of the
 119 BPs can be expressed as

$$I/F_{BP} = \frac{w_{BP}(\lambda)}{4} \frac{\mu_{0e}}{\mu_{0e} + \mu_e} [\Pi_{BP}(\lambda, g) + H(w_{BP}, \mu_{0e})H(w_{BP}, \mu_e) - 1] S(i, e, g, \bar{\theta}), \quad (8)$$

120 where H is Chandrasekhar's function and accounts for multiple scattering. The BPs, similarly to the rest
 121 of the surface, are composed of pebbles. In the BPs, pebbles are agglomerates of cometary dark terrain
 122 and water ice, thus we model them as an intimate mixture of these two end-members. This implies that
 123 the BP single scattering albedo can be expressed as a linear combination of the dark terrain (w_{DT}) and
 124 water ice (w_I) single scattering albedos:

$$w_{BP} = f_I w_I + (1 - f_I) w_{DT}, \quad (9)$$

125 where f_I is the ice fractional cross section in the BPs. In our simulation we assume a reference value of
 126 $f_I = 0.5$, in line with the estimated dust-to-water-ice volume ratio of ice-rich features on comet 67P^{10,11}.
 127 For the single scattering albedo of the comet's dark terrain we use the spectrum provided for the "bottom"
 128 region in ref.⁶. For the water ice case, in a mixture with a substantial amount of comet's dark terrain
 129 material, we can assume a constant value of $w_I = 1$. This, given the low absorption coefficient of water ice
 130 in the investigated spectral range (0.55-0.8 μm)¹², is an excellent approximation of the corresponding
 131 single scattering albedo spectrum as obtained from Hapke's modelling over a wide interval of grain sizes,
 132 from sub- μm - to mm-sized particles. As mentioned above, the spectral slope S_{VIS} has been derived after
 133 reduction of VIRTIS-M I/F measurements into single scattering albedo, which according to ref.⁶ is
 134 provided by the following general equation

$$w(\lambda) = \frac{I/F_{VIRTIS}}{\Pi_{DT}(\lambda, g)} \frac{\mu_{0e} + \mu_e}{\mu_{0e}} \frac{4}{S(i, e, g, \bar{\theta})}. \quad (10)$$

135 Given this we apply Eqs. 6 to 10 to reduce the radiance factor of an ice-hosting area into the corresponding
 136 "effective single scattering albedo", w_{eff} , obtaining

$$w_{eff} = \left((1 - f_{BP}) w_{DT}(\lambda) \Pi_{DT}(\lambda, g) + f_{BP} (w_{BP}(\lambda) [\Pi_{DT}(\lambda, g) + H(w_{BP}, \mu_{0e}) H(w_{BP}, \mu_e) - 1]) \right) / \Pi_{DT}(\lambda, g), \quad (11)$$

137 where we assumed $\Pi_{BP} = \Pi_{DT}$ and Π_{DT} is from ref.⁶. This quantity is then used to compute the spectral
 138 slope to be compared with the S_{VIS} temporal profiles measured by VIRTIS-M for the ROI 1. The best fit
 139 of the spectral slope at each given time provides the corresponding areal fraction of BP in the investigated
 140 ROI (f_{BP}).

141 For the Hapi region we also modelled the effects of a minor enrichment of water in the dark terrain. This
 142 is obtained by modifying the single scattering albedo of the dark terrain w_{DT} in Eq. 7 into w_{DT}^* , where

$$w_{DT}^* = f_I^* w_I + (1 - f_I^*) w_{DT} \quad (12)$$

143 with f_I^* representing the ice fraction.

144 4 Dust ejection rate on March 2015 and water-driven erosion in Imhotep

145 Assuming Imhotep as the main source of activity in March 2015, we estimate from cometary activity
 146 modelling (see Methods) an average daytime erosion rate E_{day} of 5.6 cm/day and a gas emission rate $Q_g(T)$
 147 of 5×10^{-6} kg/m²/s as computed at the maximum temperature experienced in Imhotep ($T = 247$ K, see
 148 methods and Supplementary Fig. 2). With this value of Q_g the maximum liftable size of the ejected dust is
 149 1 cm (ref.¹³). In this period, GIADA measured a dust flux of 20-40 kg/s for particle sizes <1 cm. The total
 150 dust flux if Imhotep were uniformly ejecting sub-cm dust can be computed as $Q_d = A \cdot \rho_d \cdot E_{day} \approx 2600$
 151 kg/s, where $A \approx 5$ km² is the Imhotep area¹⁴ and $\rho_d \approx 800$ kg/m³ is the average dust density¹⁵. This value
 152 is 65-130 times larger than the one measured by GIADA, implying that approximately only 0.8-1.5% of
 153 Imhotep is ejecting sub-cm dust.

154 5 Semi-transparent dehydrated crust scenario

155 One of the outputs of the water-driven activity model by ref.³ is the smallest size s_m of the ejected dust,
 156 ranging from about 1 mm at a heliocentric distance of 3.5 au, down to 10 μ m at 67P's perihelion (1.23 au).
 157 Assuming the surface would develop a dehydrated crust as the effect of water-ice-sublimation¹⁶⁻¹⁸, s_m
 158 would represent its thickness, being the maximum depth at which sublimation may occur without removing
 159 dust. Let's assume that this crust is sufficiently shallow and porous to be transparent to VIRTIS, which then
 160 can receive light scattered by the ice-rich layers below the crust, upon attenuation by the crust's optical
 161 thickness. In particular, for decreasing crust optical depths, the signal coming from the subsurface ice
 162 undergoes a smaller attenuation and the resulting spectral slope of the surface would become progressively
 163 bluer. If most of the nucleus has about the same ice content below the crust, for a given crust thickness,
 164 the colour observed by VIRTIS is a proxy of the nucleus ice content.

165 The thickness s_m depends directly on the surface temperature³: the higher the temperature, the smaller
 166 s_m . It follows that, for a given amount of subsurface ice, the colour measured by VIRTIS should provide a
 167 direct measurement of the crust thickness and by consequence of the surface temperature. Independent
 168 measurements of colour (VIRTIS-M VIS channel) and temperature (from thermal emission by means
 169 of the VIRTIS-M IR channel^{19,a}) evidence that this is not the case: VIRTIS in fact measures different
 170 temperatures in areas having the same colour, and different colours in areas having the same temperature.
 171 In particular, this is found when the average spectral slope in Hapi and Imhotep are compared. In August

^aWe stress here that the temperature sampled by the VIRTIS-M IR channel refers to the first some tens of microns of the surface, as reported in ref.¹⁹. Nonetheless, this quantity can be safely compared to the surface temperature at depth-zero inferred by ref.³. In fact, it can be shown that ref.³ predicts a maximum temperature drop of 0.5 K over a characteristic 100- μ m depth, being much smaller than the model uncertainty on the surface temperature (≤ 10 K) and also smaller than typical formal error on the temperature value inferred from VIRTIS-M IR channel observations (~ 1 K).

172 2014, when the comet was at approximately 3.5 au, Hapi was characterised by an average spectral slope
173 of $(17.7 \pm 0.7) \%/ (100 \text{ nm})$, as derived by averaging VIRTIS-M observations falling in an area comprised
174 in the latitude 60° - 75° and longitude 270° - 315° intervals, and the surface temperature is of the order of
175 220 K (ref.¹⁹). Such value of the spectral slope is comparable with the colour observed in Imhotep in June
176 2015 (≈ 1.45 au, after VIRTIS-M-IR cryocooler failure in May 2015), when the surface temperature would
177 be significantly higher: this can be inferred from the measured¹⁹ $T = 232$ K in Imhotep already in April
178 2015 (≈ 1.9 au). Moreover in April 2015, Imhotep's spectral slope is $S_{VIS} = (19.9 \pm 0.7) \%/ (100 \text{ nm})$, a
179 value larger than Hapi's, which is characterised by a lower temperature. The above discussions indicate
180 that the surface colour variability observed by VIRTIS cannot be explained in terms of crust thickness
181 variability over an ice-rich layer.

182 Moreover crusts thinner than the pebble size $2R$ are also inconsistent with the model³ itself. Such a
183 size $2R$ can be interpreted as the size of the dust agglomerates which have been assumed isothermal³, so
184 that the gas pressure due to diffusion inside the agglomerates overcomes the tensile strength bonding the
185 dust particles to the pebble. The pebble radius R drives the water loss flux Q_g from the nucleus³: the larger
186 the radius R , the smaller the flux Q_g , and the larger the nucleus area A required to fit the observed water
187 loss rate $Q_w = A Q_g$. In August 2014 we have $Q_w = 1.2 \text{ kg/s}$ (ref.²⁰), which, with a pebble radius $R = 5$
188 mm and the corresponding water loss flux $Q = 2.3 \times 10^{-7} \text{ kg m}^{-2} \text{ s}^{-1}$, yields $A = 5 \text{ km}^2$. Measurements of
189 Hapi's erosion have shown that on August 2014 the entire Hapi region was uniformly eroded²¹. Since
190 Hapi has $A \approx 2 \text{ km}^2$ (ref.¹⁴), we obtain that the size of the isothermal units where gas diffusion occurs
191 is at least 4 mm (all the water flux coming from Hapi). Assuming that all northern fallout deposits of
192 total $A = 10 \text{ km}^2$ (ref.¹⁴) behave as Hapi²², we get the upper limit of the size of the isothermal units of
193 20 mm. Since the best estimates of the radius of the pebbles is $R = 5$ mm (ref.²³), we can conclude that
194 the sunlit pebbles are almost perfectly isothermal. Given that the dehydration of isothermal pebbles is
195 necessarily uniform in all their volume, the crust of cometary nuclei must be at least one pebble thick.
196 This also makes it impossible to explain surface colour variability in terms of crust thickness, as a crust
197 thicker than $2R = 1 \text{ cm}$ would be completely opaque to observations at visible wavelengths.

198 6 Post-perihelion fallout effects

199 The BP temporal evolution models of Fig. 3 with WEB size $L = 0.5 - 1 \text{ m}$ provide a good match to
200 the observed behaviour up to December 2015. Later, the predicted evolution overestimates the amount
201 of BPs observed on the surface. We interpret the steeper-than-simulations BP fraction decrease after
202 perihelion as the effect of the fallout of material ejected at perihelion from the southern hemisphere and
203 then covering the BPs. Such process is not explicitly included in our surface evolution model, whereas
204 its post-perihelic effect was anticipated by requiring our simulations to match the BP temporal evolution
205 only up to September 2015 (maximum blueing). As shown in Supplementary Information section 7 and
206 Methods, the fallout material has an average water-ice content of a few percent when ejected by the
207 southern hemisphere. If the fallout material gets dehydrated to an average dust-to-water-ice mass ratio
208 $\delta > 10^3$ after ejection, once deposited on the surface (in particular on the BPs), it results in nucleus spectral
209 reddening and in a reduction of the effective estimated BP fraction. Ref.²⁵ estimates the fallout at 80%
210 of the ejected mass. Southern erosions from 4 m (ref.²⁵, eroded surface of 20% of the total one) to 10 m
211 (ref.³, eroded surface of 10% of the total one) imply an average fallout on the nucleus 0.6–0.8 m thick.
212 Starting from mid-May 2016 and up to early August 2016, the insolation conditions in Imhotep are such
213 that accumulated fallout material with $10^3 < \delta < 10^4$ (Supplementary Fig. 2) would undergo water-driven
214 erosion. This would allow fallout self-cleaning, and, with the erosion rate reported in Supplementary Fig.
215 3, we estimate a total erosion of $\approx 0.5 \text{ m}$ from mid-May 2016 to early August 2016, when water-driven

216 erosion stops. This value differs from the average amount of fallout blanketing 67P surface less than the
217 depth of the CO₂ sublimation front, indicating that the Imhotep region self-cleans from fallout by August
218 2016, thus exposing a pristine surface at the next inbound phase. This also indicates that the net erosion in
219 the Imhotep region during one orbit²¹ is mostly CO₂-driven, and that CO₂-driven erosion effectively can
220 expose WEBs starting from roughly February 2015, ensuring the replicability of the seasonal colour cycle
221 at each orbit.

222 The ongoing self-cleaning in Hapi (upper left panel in Fig. 1) exposes a much bluer interior of the
223 chunks composing the fallout than the ongoing self-cleaning in Imhotep (upper right panel in Fig. 1), i.e.
224 the fallout in Imhotep has an average δ significantly larger than in Hapi. Since Hapi is a nucleus concavity,
225 opposite to convex Imhotep, the different fallout's δ may be related to the dominant fast (ballistic) fallout
226 into Hapi with respect to a much slower (spiraling down from bound orbits²⁷) fallout into Imhotep, in fact
227 lasting many months (Fig. 3). The fast ballistic fallout into Hapi occurs during Hapi's polar night, and
228 exposes water ice in the chunk crust by thermal inversion²⁶. In the orbiting chunks of the slow spiraling
229 fallout, this process occurs at every eclipse to sunlight by the nucleus, triggering the erosion of the chunks
230 (with δ low enough) as they exit out of the eclipse back to sunlight. This process selects a slow spiraling
231 fallout much drier than the fast ballistic one.

232 7 The colour of Hapi

233 According to our result, the activity over a large part of the comet surface can be explained by discrete
234 sources (BPs) scattered in a larger dehydrating surface. The same description, however, cannot be applied
235 to the Hapi region, which in fact was uniformly active in August 2014²¹. With a surface temperature as
236 high as $T = 220$ K (ref.¹⁹), activity in Hapi is possible if the whole surface is characterised by $\delta < 10^3$
237 (ref.³). As mentioned above, in August 2014 (3.5 au), a reference value for the Hapi spectral slope
238 is $S_{VIS} = (17.7 \pm 0.7) \% / (100 \text{ nm})$. The observed colour is matched either modelling Hapi's surface
239 as a homogeneous intimate mixture of the comet dark terrain and 1-1.5% water ice ($\delta \approx 131$ -200), or
240 assuming an areal mixture of water-ice-enriched dark terrain (intimate mixture with 0.2 % volume of ice,
241 corresponding to $\delta \approx 10^3$) and 1.1-1.9% of BPs. Both these paradigms are compatible with Hapi being
242 uniformly active in August 2014, and require roughly a total ice volumetric abundance of 1% ($\approx 0.5\%$
243 in mass), in agreement with independent estimations²¹ obtained by measurements of Hapi's erosion
244 rate, which provide an ice mass fraction of $1.2 \pm 0.8\%$. Hapi and the other northern deposits on 67P, are
245 probably covered by fallout, emitted by the active southern territories close to perihelion²⁴. This process
246 is supported by our estimation of the average water-ice abundance in Hapi ($\approx 1\%$) as obtained from
247 VIRTIS-M observations, being fairly close to the amount of water ice inferred on Imhotep at perihelion.
248 Compatibly with the result of our simulations, which provides a larger fraction of BPs exposed on the
249 surface for increasing CO₂ erosion, the volumetric ice fraction in Imhotep, in fact, can be considered a
250 lower limit of the abundance of exposed ice in the southern hemisphere at perihelion, given the more
251 intense insolation conditions in the latter case¹⁷ consistent with an additional loss of water ice after
252 ejection²⁵. As all Hapi is expected to be characterised by $\delta < 10^3$, water ice has to be intimately mixed
253 with the refractory materials at sub-pebble scale across the whole surface. This requires redistribution
254 and mixing of the water ice coming from the southern BPs. In this respect, we may expect that, as
255 a consequence of the fallout, the ice-rich chunks originating from the southern BPs would be evenly
256 distributed across Hapi at spatial scales of several-chunks-size. In addition, further homogenisation of
257 the water ice distribution at sub-pebble scale can be provided by the diurnal cycle of sublimation and
258 re-condensation observed in Hapi, which acts on the scale length of the diurnal thermal skin depth, of the
259 order of few centimetres²⁶.

References

- 260 **1.** El-Maarry, M. R. *et al.* Regional surface morphology of comet 67P/Churyumov-Gerasimenko
261 from Rosetta/OSIRIS images: The southern hemisphere. *Astron. Astrophys.* **593**, A110, DOI:
262 [10.1051/0004-6361/201628634](https://doi.org/10.1051/0004-6361/201628634) (2016).
263
- 264 **2.** Acton, C. H. Ancillary data services of NASA's Navigation and Ancillary Information Facility. *Planet.*
265 *Space Sci.* **44**, 65–70, DOI: [10.1016/0032-0633\(95\)00107-7](https://doi.org/10.1016/0032-0633(95)00107-7) (1996).
- 266 **3.** Fulle, M. *et al.* How comets work: nucleus erosion versus dehydration. *Mon. Notices Royal Astron.*
267 *Soc.* **493**, 4039–4044, DOI: [10.1093/mnras/staa508](https://doi.org/10.1093/mnras/staa508) (2020).
- 268 **4.** Gundlach, B., Fulle, M. & Blum, J. On the activity of comets: understanding the gas and dust emission
269 from comet 67P/Churyumov-Gerasimenko's south-pole region during perihelion. *Mon. Notices Royal*
270 *Astron. Soc.* **493**, 3690–3715, DOI: [10.1093/mnras/staa449](https://doi.org/10.1093/mnras/staa449) (2020).
- 271 **5.** Ciarniello, M. *et al.* The global surface composition of 67P/Churyumov-Gerasimenko nucleus
272 by Rosetta/VIRTIS. II) Diurnal and seasonal variability. *Mon. Notices Royal Astron. Soc.* **462**,
273 S443–S458, DOI: [10.1093/mnras/stw3177](https://doi.org/10.1093/mnras/stw3177) (2016).
- 274 **6.** Ciarniello, M. *et al.* Photometric properties of comet 67P/Churyumov-Gerasimenko from VIRTIS-M
275 onboard Rosetta. *Astron. Astrophys.* **583** (2015).
- 276 **7.** Hapke, B. *Theory of reflectance and emittance spectroscopy* (Cambridge University Press, 2012).
- 277 **8.** Filacchione, G. *et al.* The global surface composition of 67P/CG nucleus by Rosetta/VIRTIS.
278 (I) Prelanding mission phase. *Icarus* **274**, 334–349, DOI: [10.1016/j.icarus.2016.02.055](https://doi.org/10.1016/j.icarus.2016.02.055) (2016).
279 [1602.09098](https://doi.org/10.1016/j.icarus.2016.02.055).
- 280 **9.** Coradini, A. *et al.* Virtis: An Imaging Spectrometer for the Rosetta Mission. *Space Sci. Rev.* **128**,
281 529–559, DOI: [10.1007/s11214-006-9127-5](https://doi.org/10.1007/s11214-006-9127-5) (2007).
- 282 **10.** Oklay, N. *et al.* Long-term survival of surface water ice on comet 67P. *Mon. Notices Royal Astron.*
283 *Soc.* **469**, S582–S597, DOI: [10.1093/mnras/stx2298](https://doi.org/10.1093/mnras/stx2298) (2017).
- 284 **11.** O'Rourke, L. *et al.* The philae lander reveals low-strength primitive ice inside cometary boulders.
285 *Nature* **586**, 697–701, DOI: [10.1038/s41586-020-2834-3](https://doi.org/10.1038/s41586-020-2834-3) (2020).
- 286 **12.** Warren, S. G. & Brandt, R. E. Optical constants of ice from the ultraviolet to the microwave: A
287 revised compilation. *J. Geophys. Res. (Atmospheres)* **113**, D14220, DOI: [10.1029/2007JD009744](https://doi.org/10.1029/2007JD009744)
288 (2008).
- 289 **13.** Zakharov, V. V. *et al.* Asymptotics for spherical particle motion in a spherically expanding flow.
290 *Icarus* **312**, 121–127, DOI: [10.1016/j.icarus.2018.04.030](https://doi.org/10.1016/j.icarus.2018.04.030) (2018).
- 291 **14.** Thomas, N. *et al.* Regional unit definition for the nucleus of comet 67P/Churyumov-Gerasimenko on
292 the SHAP7 model. *Planet. Space Sci.* **164**, 19–36, DOI: [10.1016/j.pss.2018.05.019](https://doi.org/10.1016/j.pss.2018.05.019) (2018).
- 293 **15.** Fulle, M. *et al.* Comet 67P/Churyumov-Gerasimenko preserved the pebbles that formed planetesimals.
294 *Mon. Notices Royal Astron. Soc.* **462**, S132–S137, DOI: [10.1093/mnras/stw2299](https://doi.org/10.1093/mnras/stw2299) (2016).
- 295 **16.** De Sanctis, M. C. *et al.* Shape and obliquity effects on the thermal evolution of the Rosetta target
296 67P/Churyumov-Gerasimenko cometary nucleus. *Icarus* **207**, 341–358, DOI: [10.1016/j.icarus.2009.](https://doi.org/10.1016/j.icarus.2009.11.009)
297 [11.009](https://doi.org/10.1016/j.icarus.2009.11.009) (2010).
- 298 **17.** Keller, H. U. *et al.* Insolation, erosion, and morphology of comet 67P/Churyumov-Gerasimenko.
299 *Astron. Astrophys.* **583**, A34, DOI: [10.1051/0004-6361/201525964](https://doi.org/10.1051/0004-6361/201525964) (2015).

- 300 **18.** Hu, X. *et al.* Seasonal erosion and restoration of the dust cover on comet 67P/Churyumov-
301 Gerasimenko as observed by OSIRIS onboard Rosetta. *Astron. Astrophys.* **604**, A114, DOI:
302 [10.1051/0004-6361/201629910](https://doi.org/10.1051/0004-6361/201629910) (2017).
- 303 **19.** Tosi, F. *et al.* The changing temperature of the nucleus of comet 67P induced by morphological and
304 seasonal effects. *Nat. Astron.* **3**, 649–658, DOI: [10.1038/s41550-019-0740-0](https://doi.org/10.1038/s41550-019-0740-0) (2019).
- 305 **20.** Gulkis, S. *et al.* Subsurface properties and early activity of comet 67P/Churyumov-Gerasimenko.
306 *Science* **347**, aaa0709, DOI: [10.1126/science.aaa0709](https://doi.org/10.1126/science.aaa0709) (2015).
- 307 **21.** Cambianica, P. *et al.* Time evolution of dust deposits in the Hapi region of comet 67P/Churyumov-
308 Gerasimenko. *Astron. Astrophys.* **636**, A91, DOI: [10.1051/0004-6361/202037485](https://doi.org/10.1051/0004-6361/202037485) (2020).
- 309 **22.** Cambianica, P. *et al.* Long-term measurements of the erosion and accretion of dust deposits on comet
310 67P/Churyumov-Gerasimenko with the OSIRIS instrument. *Mon. Notices Royal Astron. Soc.* DOI:
311 [10.1093/mnras/stab950](https://doi.org/10.1093/mnras/stab950) (2021). Stab950, [https://academic.oup.com/mnras/advance-article-pdf/doi/10.](https://academic.oup.com/mnras/advance-article-pdf/doi/10.1093/mnras/stab950/37008172/stab950.pdf)
312 [1093/mnras/stab950/37008172/stab950.pdf](https://academic.oup.com/mnras/advance-article-pdf/doi/10.1093/mnras/stab950/37008172/stab950.pdf).
- 313 **23.** Blum, J. *et al.* Evidence for the formation of comet 67P/Churyumov-Gerasimenko through gravita-
314 tional collapse of a bound clump of pebbles. *Mon. Notices Royal Astron. Soc.* **469**, S755–S773, DOI:
315 [10.1093/mnras/stx2741](https://doi.org/10.1093/mnras/stx2741) (2017). [1710.07846](https://doi.org/10.1093/mnras/stx2741).
- 316 **24.** Keller, H. U. *et al.* Seasonal mass transfer on the nucleus of comet 67P/Chuyumov-Gerasimenko.
317 *Mon. Notices Royal Astron. Soc.* **469**, S357–S371, DOI: [10.1093/mnras/stx1726](https://doi.org/10.1093/mnras/stx1726) (2017). [1707.06812](https://doi.org/10.1093/mnras/stx1726).
- 318 **25.** Fulle, M. *et al.* The refractory-to-ice mass ratio in comets. *Mon. Notices Royal Astron. Soc.* **482**,
319 3326–3340, DOI: [10.1093/mnras/sty2926](https://doi.org/10.1093/mnras/sty2926) (2019).
- 320 **26.** De Sanctis, M. C. *et al.* The diurnal cycle of water ice on comet 67P/Churyumov-Gerasimenko.
321 *Nature* **525**, 500–503, DOI: [10.1038/nature14869](https://doi.org/10.1038/nature14869) (2015).
- 322 **27.** Bertini, I. *et al.* The backscattering ratio of comet 67P/Churyumov-Gerasimenko dust coma as seen
323 by OSIRIS onboard Rosetta. *Mon. Notices Royal Astron. Soc.* **482**, 2924–2933, DOI: [10.1093/mnras/](https://doi.org/10.1093/mnras/sty2843)
324 [sty2843](https://doi.org/10.1093/mnras/sty2843) (2019).